Nuclear Engineering and Design 392 (2022) 111762

Contents lists available at ScienceDirect

Nuclear Engineering and Design

journal homepage: www.elsevier.com/locate/nucengdes

Multiphysics modelling of gaseous fission products in the Molten Salt Fast Reactor

Federico Caruggi [a], Antonio Cammi [a,*], Eric Cervi [a,b], Andrea Di Ronco [a], Stefano Lorenzi [a]

[a] Department of Nuclear Engineering – Politecnico di Milano, Via la Masa, 34, Milan 20156, Italy
[b] Nuclear Research and Consultancy Group NRG, Westerduinweg, 3, LE Petten 1755, The Netherlands

ARTICLE INFO

Keywords:
Multiphysics
OpenFOAM
Molten Salt Fast Reactor
Gaseous fission products
Helium bubbling

ABSTRACT

The Molten Salt Fast Reactor (MSFR) is a nuclear reactor concept under development in the framework of the H2020-Euratom project SAMOSAFER. Given its peculiar characteristics as a circulating-fuel reactor, new simulation tools need to be developed and tested for its study. In this work, a multiphysics solver previously developed in OpenFOAM is extended with new functionalities for the analysis of this reactor design. The main focus is the modelling of the behavior of Gaseous Fission Products (GFPs) inside the core and their interactions with a helium bubbling system, foreseen to remove both GFPs and metallic fission products through flotation. On the basis of an Euler-Euler solver able to model the presence of the two phases – namely the liquid fuel and the gaseous bubbles – , a multi-component mixture approach is adopted to simulate the behavior of GFP species in the core, with particular focus on their production, consumption, transport, mass exchange and removal to the off-gas system. The new capabilities are tested on both 2D and 3D MSFR cases, considering Xe-135 as reference nuclide, with focus on the efficiency of the bubbling system in the removal of GFPs from the salt. As main figure of merit of the removal capability, a cycle time related to the extraction of the specie from the system is defined and calculated for different conditions of helium injection. This work constitutes a further advancement in the development of the MSFR concept, extending the modelling capabilities of the previous multiphysics solver. Reliable estimation of the evolution of the gaseous fission products in the reactor core and the related effect of the helium bubbling system is a fundamental requirement for the analysis of the radioactive source term and for the prediction of the overall operating conditions of this innovative nuclear system.

1. Introduction

The Molten Salt Fast Reactor (MSFR) is a circulating-fuel reactor concept currently under development in the framework of H2020 EURATOM project SAMOSAFER (https://samosafer.eu/). It is based on the Thorium fuel cycle and it features a liquid mixture of fluoride salts which acts simultaneously as fuel and coolant. This innovative reactor concept offers several advantages with respect to conventional nuclear systems, introducing at the same time new design features and challenges. Among them is the helium bubbling system, an in-core apparatus foreseen to inject a flow of helium bubbles in the mixture, in order to extract non-soluble fission products - in gaseous and metallic form - from the fuel (Delpech et al., 2009). New simulation tools are therefore needed to support the design of molten salt reactors (Betzler et al., 2019). In particular, the helium bubbling system plays a fundamental role in the estimation of the source term and in the identification of the location of the radioisotopes in the system.

For the analysis of the MSFR, different approaches have been followed in the past at Politecnico di Milano, to account for the dynamics of the reactor both from a neutronics and thermal–hydraulics point of view. The first attempt featured a combination of zero-dimensional approach for the thermal–hydraulic modelling and point-kinetics equations for the neutronics (Cammi et al., 2011). Following this, newer models were developed employing finite element multiphysics codes, with multi-group diffusion equations for neutronics and a single-phase incompressible solver for the thermal–hydraulics part (Fiorina et al., 2014), able to perform simulations on simplified 2D models of the MSFR. As a final step, a complete 3D model of the reactor has been constructed, and a multiphysics solver has been developed (Cervi et al., 2017; Cervi et al., 2019), based on the OpenFOAM library (Weller et al.,

* Corresponding author.
E-mail addresses: federico.caruggi@mail.polimi.it (F. Caruggi), antonio.cammi@polimi.it (A. Cammi), eric.cervi@polimi.it (E. Cervi), andrea.dironco@polimi.it (A. Di Ronco), stefano.lorenzi@polimi.it (S. Lorenzi).

https://doi.org/10.1016/j.nucengdes.2022.111762
Received 17 October 2021; Received in revised form 1 April 2022; Accepted 2 April 2022
Available online 21 April 2022

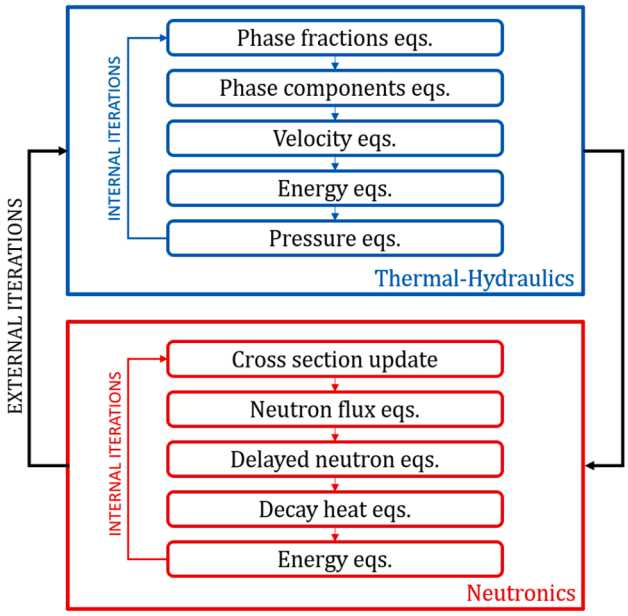

Fig. 1. Structure of the solver with subdivision of time step in cycles.

1998), which features diffusion and SP_3 neutron transport models, including delayed neutrons and decay heat precursors transport. The thermal–hydraulics module follows a Computational Fluid Dynamics (CFD) approach with the possibility to model a single phase (only the liquid fuel) or the presence of the additional gaseous helium phase, thanks to an Euler-Euler formulation. The influence of helium bubbles on the removal of fission products, however, has not been investigated yet and is the subject of the this work.

In previous studies, the behavior of gaseous fission products has been modelled considering the effects of the different gas sources and sinks present in the Molten Salt Reactor Experiment (MSRE) and implemented in a system code (Roelofs and Stempniewicz, 2021). In Price et al. (2020) and Price et al. (2020), the impact of xenon has been studied and a dynamic model was developed and tested against experimental data from ORNL. In the MSRE, the main issue to cope with was the xenon poisoning and the removal of the Xe was achieved through a stripping device (spray ring) located in the fuel pump bowl (Engel and Steffy, 1971). In addition to decay and burnup that are necessarily present as sink term, another removal term for the xenon was the migration to the graphite. It seems clear that the MSRE system is quite different from the one foreseen in the MSFR, due to the absence of graphite and the presence of a in-core helium flow (whereas in the MSRE the helium was injected ex-core). The latter, combined to the absence of internals and the shape of the MSFR, makes the issue related to the transport of gaseous fission products and the interactions with helium bubble flow a three dimensional problem that should be tackled with a CFD approach. This choice allows also for the analysis of the system taking into account the real bubble distribution inside the MSFR core, rather than considering an average circulating void fraction in the volume.

In fuel depletion codes for MSRs (Aufiero et al., 2013), the effect of the helium bubbling system on the gaseous fission products has been modelled following a formulation analogous to radioactive decay of the interested nuclides, through the use of a suitable characteristic time constant. This parameter represents the efficiency of the helium bubbling system in the extraction of the fission products from the fuel mixture to the helium flow (and then to the off gas system). A preliminary estimation of this value was given in the order of magnitude of tens of seconds, with a proposed reference value of 30 s (Aufiero et al., 2013). A more accurate estimate of the efficiency of the helium bubbling system is required, especially if we consider that the efficiency of this system depends on several factors (e.g. helium mass flow rate, injection and removal locations, size and shape of the reactors).

This paper presents a further development of the previously available multiphysics solver to introduce the capability to model the behavior of the gaseous fission products in the Molten Salt Fast Reactor, with regards to their production, transport and consumption in the fuel mixture and, most importantly, their interactions with the helium bubbles. The simulations performed with this new and improved tool allow the computation of the characteristic time mentioned above, evaluating the efficiency of the bubbling system in the removal of gaseous fission products in consideration of a realistic bubble distribution and taking into account the phenomenon of mass transfer between the liquid and gaseous phases. Physical parameters needed for the formulation of the problem have been collected from past experimental studies performed at Oak Ridge National Laboratory (ORNL) (Kedl and Houtzeel, 1967; Peebles, 1968). Working on thermal nuclear systems as the MSRE and the Molten Salt Breeder Reactor (MSBR), much focus was put on the behavior of some gaseous fission products, as for example xenon, acting as a neutronic poison inside the fuel mixture. The modelling approaches and numerical results employed at the time can still be considered, as of today, relevant guidelines in the analysis of new systems as well, as is the case of the MSFR.

The remainder of this paper is organized as follows. After a brief description of the previous solver capabilities in Section 2, the new features are presented in Section 3, with references to both the analytical formulation and the code implementations. These added features are then tested against an analytical model in Section 4, in order to verify the reliability of the models. Subsequently, in Section 5 the upgraded computational tool is employed for simulations on the MSFR system, for both a 2D and a 3D model, testing the new capabilities on representative geometries and performing the analyses mentioned above on the behavior of gaseous fission products in combination with the helium bubbling system.

2. The OpenFOAM multiphysics solver for MSR

The starting point of the modelling and simulation of the gaseous fission product in MSR is a solver developed in the past (Cervi et al., 2017; Cervi et al., 2019) for the neutronics and the thermal hydraulics analysis of the MSFR. In particular, the solver is already able to deal with two-phase flows and it has been used to study the effect of the helium bubbling system on neutronics (Cervi et al., 2019). The algorithm divides each time step in two different cycles, as shown in Fig. 1. The first one employs a thermal–hydraulics sub-solver, based on the pre-existing OpenFOAM solver "reactingTwoPhaseEulerFoam", in order to consider the fluid dynamics of the compressible liquid and the gaseous bubbles. The second cycle concerns the neutronics of the system and follows one of two selectable modelling approaches: one based on multi-group diffusion, the other based on the multi-group SP_3 approximation (Cervi et al., 2019).

2.1. Thermal hydraulics sub-solver

The standard two-phase OpenFOAM solver "reactingTwoPhaseEulerFoam" is based on the Euler-Euler approach, in which both phases are treated as continua interpenetrating each other (Rusche, 2002). For both phases, continuity equations are formulated according to an Eulerian description and the topology is thus defined through a phase fraction quantity, corresponding to the volumetric portion of the finite volume discretization cell occupied by the dispersed phase. The algorithm starts with the solution of the macroscopic mass conservation equation for each phase, followed by the mass balance for each component of the single phase (further details are given in Section 3). Next, the macroscopic momentum and energy balance equations are solved, following the formulations presented in Ishii et al. (2011); Marschall (2011). In this formulation, the same value of pressure is used

for both phases. Explicit terms representing the momentum and heat transfer between the two phases are considered due to the non-linearity of the system and the need for closure equations. Empirical models and correlations are thus employed in the algorithm to determine the single contributions that add up to the collective terms, corresponding to single effects acting at the interface between the phases (e.g. for the momentum transfer, drag, lift, turbulent dispersion and virtual mass forces (Lathouwers, 1999)). Among the main closure relations and correlations available in literature, both for momentum and heat transfer, this work follows the choices made in a previous work (Cervi, 2020). In particular, the explicit terms in the momentum balance equation are treated with the following correlations:

- For virtual mass forces, a constant coefficient correlation is chosen, with $C_{VM} = 0.5$ (Rusche, 2002)
- Lift is not considered, following the assumption that the bubbles are sufficiently small in size to neglect the effect of vorticity on the momentum transfer between the two phases
- Turbulent dispersion is neglected as well
- The drag coefficient is evaluated by use of the Schiller-Naumann correlation (Schiller and Naumann, 1933):

$$C_D = \begin{cases} \dfrac{24\left(1 + 0.15\mathrm{Re}_b^{0.687}\right)}{\mathrm{Re}_b} & \text{for} \quad \mathrm{Re}_b < 1000 \\ 44 & \text{for} \quad \mathrm{Re}_b \geqslant 1000 \end{cases} \tag{1}$$

The Reynolds number employed here is the one referring to a single bubble transported by the liquid, so that the characteristic length is the diameter of the bubble and the velocity is the difference between that of the bubble and the one of the liquid some distance away (Rhodes, 2008):

$$\mathrm{Re}_b = \frac{|\mathbf{u}_g - \mathbf{u}_l| d_b}{\nu_l} \tag{2}$$

The heat transfer between the phases is modelled following the Ranz-Marshall correlation (Ranz and Marshall, 1952):

$$\mathrm{Nu} = 2 + 0.6\,\mathrm{Re}_b^{1/2}\mathrm{Pr}^{1/3} \tag{3}$$

The standard k-ϵ model is employed to account for turbulence of the fuel, following the RANS approach. The bubble diameter is evaluated by use of an isothermal power law, considering the dependence on pressure:

$$d_b = d_0\left(\frac{p_0}{p}\right)^{1/3} \tag{4}$$

where the reference diameter is $d_0 = 3$ mm, at the pressure of $p_0 = 1$ atm.

With respect to the standard version of the twoPhaseEulerFoam solver, the thermal–hydraulic sub-solver employed in this work presents some additional terms. Namely, the solver introduces a source term in the mass conservation equation of the gaseous phase, accounting for the bubble injection/extraction process, and a source term in the energy balance equation of the liquid, representing the contribution of the volumetric power sources due to fission and decay heat, calculated by the neutronics sub-solver.

2.2. Neutronics sub-solver

In the neutronics sub-solver, after the update of the cross section terms, the algorithm proceeds with the solution of the equations for the neutron population balance. The solver allows for a choice between two different approaches: a multi-group neutron diffusion model and a multi-group SP_3 neutron transport model (Cervi et al., 2019), both following an iterative solution among the energy groups (Cervi et al., 2017; Cervi et al., 2019). In this work, the diffusion model is employed, simulating the presence of the external reflectors and the blanket salt through the use of albedo boundary conditions. The six-groups constants are generated with the Monte Carlo code for reactor analysis and burnup calculations Serpent-2 (Leppänen et al., 2015),using the JEFF-3.1.1 library (Santamarina et al., 2009). Details on the energy group subdivision, together with the coefficients employed for the albedo boundary conditions, can be found in Cervi (2020).

Suitable balance equations are solved for both the delayed neutron precursors and the decay heat precursors, considering terms of diffusion and advection in order to account for the transport of the species in the fuel motion. The solver is provided also with a routine to calculate the multiplication factor, solving the eigenvalue problem with a power iteration method. From the neutronics point of view, a user-defined choice is given to select between the time-dependent mode or an eigenvalue mode for the simulations. The analyses of this work are all based on the eigenvalue calculation for the neutronics part of the problem.

2.3. Coupling between sub-solvers

The results from neutronics influence the thermal–hydraulic part of the problem through a power source term figuring in the energy equation, which is computed as sum of fission power and decay heat. At the same time, the neutronic equations are influenced by thermal–hydraulics through the feedback effects of temperature, density and void fraction. The macroscopic cross sections of any reaction for each energy group are updated each time-step, with an expression constituted by a constant term, an additive logarithmic term accounting for the effect of temperature, and two multiplicative terms, one representing the effect of density and one for void fraction:

$$\Sigma_{i,j} = \left[\Sigma_{i,j}^0 + A_{i,j}\, log\frac{T_{fuel}}{T_{ref}}\right] \frac{\rho_{fuel}}{\rho_{ref,fuel}}(1 - \alpha_b) \tag{5}$$

The coefficients $A_{i,j}$ are obtained with Serpent-2 runs through logarithmic interpolation between the values corresponding to two different temperature levels, which are chosen as representative of the problem (Cervi et al., 2019).

3. Gaseous Fission Products modelling

For the removal of Gaseous Fission Products (GFPs) in the MSFR, an in-core system based on helium bubbling has been proposed (Delpech et al., 2009). In previous works (Cervi et al., 2017; Cervi et al., 2019), a model to account for the presence of the second phase generated by the helium stream has been developed. Nevertheless, this simulation tool lacked the ability to describe the interaction between the bubble and the GFPs in the core and, most of all, their behavior in view of the transport to the off-gas system. This requires the modelling of the production, consumption, transport, mass exchange and removal of the GFPs. Despite the less relevant importance in fast system as the MSFR, in this work, the single nuclide Xe-135 is taken as reference for the GFPs due to characterization performed for thermal reactors (Kedl and Houtzeel, 1967; Engel and Steffy, 1971). On the other hand, the approach can be easily extended to any other GFPs.

3.1. Governing equations

In order to grant a degree of flexibility in the OpenFOAM multiphysics solver, a multi-component approach allowing for the definition of different chemical species within each phase has been chosen. Specifically, xenon (or any other GFP) can be introduced as an additional component in both the liquid and gaseous phases. The generation of the fission product takes place directly in the mixture with the salt and the migration to the helium gas bubbles is considered with appropriate mass transfer models. Within the algorithm structure, as mentioned in Section 1, the presence of multiple species in each phase introduces a new set of balance equations to be solved, describing the evolution of the

concentration of the components and accounting for terms of production, transport and consumption. A general formulation for species i (which can be salt, xenon or helium) in phase k (liquid or gaseous) is

$$\frac{\partial \alpha_k C_{i,k}}{\partial t} + \nabla\cdot\left(\alpha_k \mathbf{u}_k C_{i,k}\right) - \nabla\cdot\left(\alpha_k D_k \nabla\left(C_{i,k}\right)\right) = \frac{dm_{i,k}}{dt} \tag{6}$$

where $C_{i,k}$ is the concentration of specie i in phase k (expressed in kg/m^3) and $\frac{dm_{i,k}}{dt}$ denotes the mass transfer of the species to or from the phase. The diffusivity coefficient for the components of a phase, D_k, can be calculated from the dimensionless Schmidt number, Sc, as

$$D_k = \frac{\mu_k}{\rho_k \mathrm{Sc}_k} \tag{7}$$

The rate of mass transfer of species i in phase k can be computed as:

$$\frac{dm_{i,k}}{dt} = K_{i,k} a \left(C^*_{i,k} - C_{i,k}\right) \tag{8}$$

where $C^*_{i,k}$ denotes the saturation concentration at the interface, $K_{i,k}$ is the mass transfer coefficient, and a represents the interfacial area of exchange per unit volume, dependent on the pair of phases where the component is present. In the case of a liquid–gas system, this last term is calculated from the bubble diameter (d_b) as

$$a_{liquid/gas} = \frac{6\,\alpha_g}{d_b} \tag{9}$$

The solver requires suitable models to compute the saturation concentration and the mass transfer coefficient of Eq. (8) for each component in each phase. The past experimental works of the Oak Ridge National Laboratory on the design of the MSRE and the MSBR are useful as indications for the basis of this formulations. Following the approach used for the analyses on the behavior of xenon in the molten salt reactors, presented in Kedl and Houtzeel (1967); Engel and Steffy (1971), an Henry-like behavior is chosen. The saturation concentration at the interface for xenon in the liquid phase is thus computed from its concentration in the gaseous one as

$$C^*_{Xe,l} = H\, C_{Xe,g} \tag{10}$$

where H is the dimensionless Henry coefficient. The value for this parameter is $H = 2.08{\cdot}10^{-4}$, retrieved from Kedl and Houtzeel (1967).

To calculate the mass transfer coefficient, the chosen model exploits the definition of a dimensionless group, the Sherwood number, representing the ratio between convective and diffusive mass transfer:

$$K_{i,k} = \frac{\mathrm{Sh}\, D_k}{d_b} \tag{11}$$

The Sherwood number is generally obtained through empirical correlations, tailored on the particular conditions of the flow in the case of interest. These models can be derived from both analytical and experimental studies and, for the case of gaseous bubbles in liquid flows, they generally result in an analogy with the heat transfer correlations (Dittus-Boelter-like, where Nu and Pr are replaced respectively by Sh and Sc), employing the bubble Reynolds number defined in Eq. (2). Among the available correlations for the Sherwood number, the one proposed by Higbie (1935) is chosen:

$$\mathrm{Sh} = 1.13\ \mathrm{Re}^{1/2}\mathrm{Sc}^{1/2} \tag{12}$$

This particular formulation has been developed for the case of free-rise of bubbles in a liquid stream, which is a condition somewhat similar to the MSFR environment, and it has been already considered in the works of ORNL (Peebles, 1968). The main limitation is that this approach refers to a laminar stream, while the regime of flow for the MSFR is expected to be turbulent. Being currently in the absence of experimental data regarding this matter, however, the approximation can be considered acceptable.

3.2. OpenFOAM implementation

To solve the mass balance of components in each phase, the OpenFOAM solver employs species transport equations similar to Eq. (6). The solver used in this work is developed for the treatment of compressible flow, so the species mass fraction in the phase (with units of kg/kg) is considered instead of the volumetric concentration:

$$Y_{i,k} = \frac{C_{i,k}}{\rho_k} \tag{13}$$

The proper expression for the balance equations in the solver is thus

$$\frac{\partial \alpha_k \rho_k Y_{i,k}}{\partial t} + \nabla\cdot\left(\alpha_k \rho_k \mathbf{u}_k Y_{i,k}\right) - \nabla\cdot\left(\frac{\alpha_k \mu_k}{\mathrm{Sc}_k}\nabla\left(Y_{i,k}\right)\right) = \frac{dm_{i,k}}{dt} \tag{14}$$

In order to simulate the behavior of xenon and other GFPs in the system, some more terms need to be supplied, modelling their production and consumption. In this work, as already stated, only the isotope 135 of xenon is considered as reference, but the considerations made here can be easily adapted for any gaseous fission product. In a reactor, Xe-135 is produced both as a direct fission product (with a certain yield), and as result of the decay of other fission products, I-135 and Te-135, which are precursors in its decay chain. As a first approximation in the modelling, it is possible to neglect the presence of the other nuclides, and consider as if all the xenon was produced by fission, with an equivalent cumulative yield. A source term is thus inserted in the transport equation relative to the liquid phase, in a form of direct proportionality with the fission rate of the system. The consumption of xenon and other GFPs is modelled in this work with the simulation of neutron capture and decay phenomena. The component is modelled as if it disappears in both cases, without taking into account the products of these reactions. The capture term is considered only for the liquid phase through the use of a suitable cross section, evaluated by means of the Serpent-2 code (Leppänen et al., 2015). The decay term is present in both phases.

The final xenon balance equations implemented in the solver are, for liquid and gaseous phase respectively,

$$\begin{aligned}\frac{\partial \alpha_l \rho_l Y_{Xe,l}}{\partial t} &+ \nabla\cdot\left(\alpha_l \rho_l \mathbf{u}_l Y_{Xe,l}\right) - \nabla\cdot\left(\frac{\alpha_l \mu_l}{\mathrm{Sc}_l}\nabla\left(Y_{Xe,l}\right)\right) \\ &= S_{Xe} - \alpha_l \rho_l \left(\lambda + \sum_n \left(\sigma_{c,n}\varphi_n\right)\right) Y_{Xe,l} + \frac{dm_{Xe,l}}{dt}\end{aligned} \tag{15}$$

$$\begin{aligned}\frac{\partial \alpha_g \rho_g Y_{Xe,g}}{\partial t} &+ \nabla\cdot\left(\alpha_g \rho_g \mathbf{u}_g Y_{Xe,g}\right) - \nabla\cdot\left(\frac{\alpha_g \mu_g}{\mathrm{Sc}_g}\nabla\left(Y_{Xe,g}\right)\right) \\ &= -\alpha_g \rho_g \lambda Y_{Xe,g} + \frac{dm_{Xe,g}}{dt}\end{aligned} \tag{16}$$

$$\frac{dm_{Xe,l}}{dt} = -\frac{dm_{Xe,g}}{dt} = \frac{6\,\alpha_g\,\mathrm{Sh}}{d_b^2} D_l \rho_l \left(H Y_{Xe,g}\frac{\rho_g}{\rho_l} - Y_{Xe,l}\right) \tag{17}$$

$$S_{Xe} = y_{Xe}\frac{m_{mol}}{N_{Av}}\sum_n \left(\Sigma_{f,n}\varphi_n\right) \tag{18}$$

where m_{mol} is the molar mass of Xe-135 and N_{Av} is the Avogadro number. It is worth to point out that there is no explicit term in these equations to account for the removal of xenon from the system through the bubbling system. This is because, as mentioned in Section 2.1, the extraction is modelled at the mass conservation level, with a linear sink term which is active only in a selected region of the geometry. Thus the removal mechanism acts on the whole gaseous phase, and not on the single helium and xenon components.

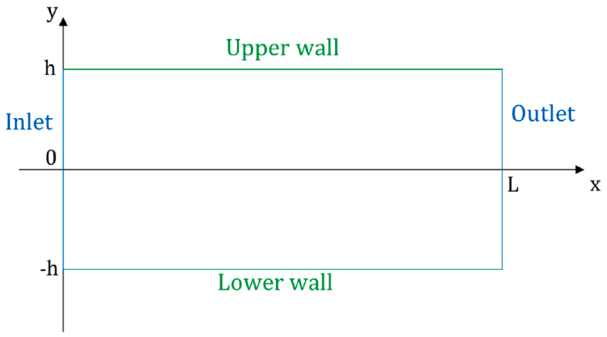

Fig. 2. Geometry for analytical benchmark.

Table 1
Mesh parameters.

Parameter	Symbol	Value	Units
Height of channel	$2h$	0.1	m
Length of channel	L	1.0	m
Depth of channel	dz	0.01	m
Mesh elements in direction x	n_x	50	–
Mesh elements in direction y	n_y	50	–
Mesh elements in direction z	n_z	1	–

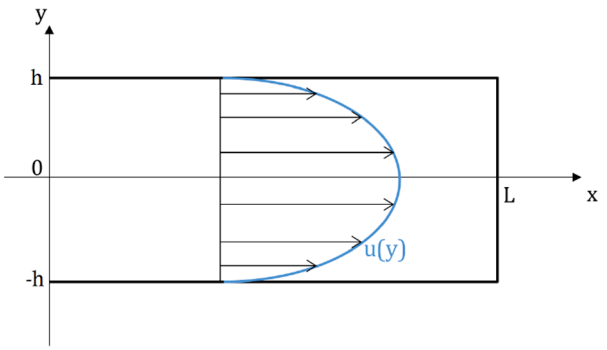

Fig. 3. Assumed parabolic profile of velocity.

4. Analytical verification

In order to verify the implementation of the new modelling features related to the GFP in the multiphysics OpenFOAM solver, a first verification is performed to test the simulation outcomes against analytical results. To this aim, following the logic of a similar case of study (Ronco et al., 2021), a simple benchmark case is defined for the mass transfer process, and the OpenFOAM results are tested against the exact analytical solution.

4.1. Geometry

The geometry chosen for the benchmark case is a two-dimensional rectangular domain, simulating a pipe section of height $2h$ and length L (Fig. 2). The salt flow is directed towards the positive direction of the x axis, so that the left vertical segment represents the inlet and the right one the outlet, while the horizontal segments are the pipe walls.

The pipe is directed horizontally to neglect the effect of gravity, simplifying the calculations. The intersection of the axes is positioned at the half height of the pipe, in order to exploit the symmetry later on. The length L is significantly larger than the height $2h$, so that inlet/outlet effects can be ignored by considering the results in the central transverse sections (the values selected for the parameters are reported in Table 1).

4.2. Derivation of analytical solutions

4.2.1. Single-phase case

The general formulation of the problem refers to the advection–dispersion equation with the addition of a source and a decay term reads:

$$\frac{\partial C}{\partial t}+\nabla\cdot\left(\mathbf{u}C\right)=\nabla\cdot\left(D\nabla C\right)-\lambda C+S \tag{19}$$

This general equation is simplified by considering a two-dimensional steady-state case, so that there is no dependence on the z coordinate and the time derivatives are removed from the expression. The flow is developed from an imposed fixed pressure gradient along the longitudinal axis of the geometry, x. In order to simplify the analytical derivation, the gradient is chosen to be low enough that pressure can be approximated as uniform throughout the domain. Additionally, no energy sources or sinks are defined, so that the temperature along the tube is uniform as well. These conditions grant that the thermophysical properties of the species involved remain constant throughout the simulations. The flow, directed along the positive x axis, is considered to be fully developed, so that the velocity field depends only on the y coordinate. For the sake of simplicity, a laminar situation is considered, leading to the common parabolic profile (h is the half-height of the domain), as seen in Fig. 3:

$$u_x\left(x,y\right)=\frac{3}{2}\overline{u}\left(1-\left(\frac{y}{h}\right)^2\right) \tag{20}$$

The hypothesis of laminar flow implies a constant value for the diffusivity coefficient, further simplifying the problem in order to obtain an analytical solution. Additionally, in consideration of steady state conditions, the phenomenon of transport is taken as fully developed, so that there is no variation of concentration of the specie along the longitudinal direction of the tube. This latter hypothesis removes all the remaining dependencies on the x axis in the equation, making the problem formulation effectively one-dimensional.

Considering all the assumptions above, the original equation (Eq. (19)) can be rewritten, in explicit Cartesian coordinates, as:

$$D\frac{\partial^2 C}{\partial y^2}-\lambda C+S=0 \tag{21}$$

The problem can also be formulated more conveniently upon the definition of appropriate dimensionless quantities:

$$\widetilde{y}=\frac{y}{h} \tag{22}$$

$$\Lambda=\frac{\lambda h^2}{D} \tag{23}$$

$$\widetilde{S}=\frac{Sh^2}{D} \tag{24}$$

The final equation to be solved is thus:

$$\frac{\partial^2 C}{\partial \widetilde{y}^2}-\Lambda C+\widetilde{S}=0 \tag{25}$$

In order to solve the problem, suitable boundary conditions need to be defined. Being the problem only dependent on the dimensionless coordinate $\widetilde{y}$, conditions are required just for the upper and lower walls of the domain. The analysis is performed for both Neumann and Dirichlet conditions:

$$\text{Neumann}: \quad \frac{\partial C}{\partial \widetilde{y}}=0;\ \widetilde{y}=\pm 1 \tag{26}$$

$$\text{Dirichlet}: \quad C(\widetilde{y})=0;\ \widetilde{y}=\pm 1 \tag{27}$$

Considering Neumann conditions, the solution is readily obtainable

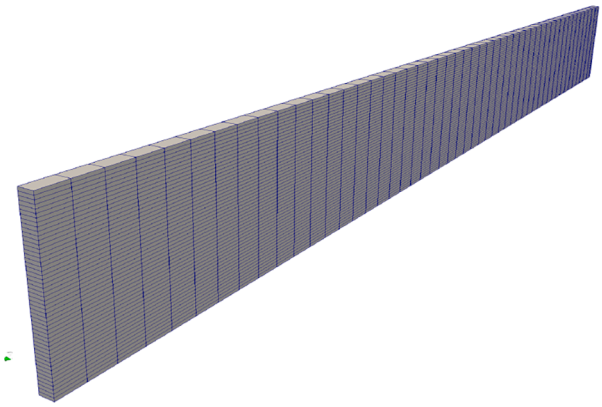

Fig. 4. Mesh for analytical model.

Table 2
Main parameters for the analytical model.

Parameter	Symbol	Value	Units
Xe diffusivity in salt	D	$1.29{\cdot}10^{-9}$	m^2/s
Henry's law coefficient	H	$2.08{\cdot}10^{-4}$	–
Xe decay constant	λ	$2.1066{\cdot}10^{-5}$	1/s
Fission rate	fR	$1{\cdot}10^{15}$	$1/m^3$ s
Xe cumulative yield	y_{Xe}	0.05875	–
Xe molar mass	m_{mol}	0.135	kg/mol

and corresponds to a flat profile (constant value), in the form of:

$$C\left(\tilde{y}\right) = \frac{\tilde{S}}{\Lambda} \tag{28}$$

For what concerns the case of Dirichlet conditions, instead, the solution is found to be (Polyanin and Zaitsev, 2002):

$$C\left(\tilde{y}\right) = \frac{\tilde{S}}{\Lambda}\left[1 - \frac{e^{\sqrt{\Lambda}\tilde{y}} + e^{-\sqrt{\Lambda}\tilde{y}}}{e^{\sqrt{\Lambda}} + e^{-\sqrt{\Lambda}}}\right] \tag{29}$$

It is worth noticing that, as mentioned before, in order to account for the compressibility of the fluids, OpenFOAM makes use of the mass fraction of the component, instead of its concentration in volume used in the previous equations. In this analytical treatment, however, the initial hypotheses of uniform temperature and pressure imply that the density of the liquid is a constant value, so that the conversion between C and Y can be done directly on the final results.

4.2.2. Two-phase case

Considering the presence of the gaseous phase as well, the formulation of the problem requires an additional equation, coupled with the first one by means of a mass transfer term following a Henry-like approach. Thanks to mass conservation, the mass transfer terms cancel out when the two equations are summed. Additionally, the phase fractions have to be introduced as well, which are taken as uniform and constant for this problem. The complete system then reads as:

$$\begin{cases} \dfrac{\partial \alpha_l C}{\partial t} + \nabla\cdot\left(\alpha_l \mathbf{u} C\right) - \nabla\cdot\left(D\nabla\alpha_l C\right) = S - \lambda\alpha_l C + KA\left(HC_g - C\right) \\ \dfrac{\partial \alpha_g C_g}{\partial t} + \nabla\cdot\left(\alpha_g \mathbf{u}_g C_g\right) - \nabla\cdot\left(D_g\nabla\alpha_g C_g\right) = -\lambda\alpha_g C_g - KA\left(HC_g - C\right) \end{cases} \tag{30}$$

For the sake of simplicity, an additional hypothesis is made with respect to the ones mentioned for the single-phase case: the phenomenon of transport is neglected in the gaseous phase. This allows for a simple solution of the gas equation, giving a direct relationship between the concentrations in the two phases:

$$C_g = \frac{KA}{\alpha_g\lambda + KAH} C \tag{31}$$

Upon substitution of this expression, the problem simplifies to a single equation for the liquid phase, in the form:

$$D\frac{\partial^2 C}{\partial y^2} - \left(\lambda + \beta\right)C + \frac{S}{\alpha_l} = 0 \tag{32}$$

where

$$\beta = -\frac{KA}{\alpha_l}\left(\frac{KAH}{\alpha_g\lambda + KAH} - 1\right) \tag{33}$$

From this point on, the steps for the manipulation of the equation are analogous to the ones made for the case of single phase, with the presence of the additional term deriving from mass transfer. The final form of the equation, with the appropriate dimensionless quantities reads as:

$$\frac{\partial^2 C}{\partial \tilde{y}^2} - \left(\Lambda + B\right)C + \tilde{S} = 0 \tag{34}$$

where $\tilde{S}$ this time incorporates also the phase fraction, and the last dimensionless quantity, B, is defined as:

$$B = \frac{\beta h^2}{D} \tag{35}$$

As in the previous case, the solution is calculated for both Neumann and Dirichlet boundary conditions. For the former, a constant profile is obtained again, in the form of:

$$C\left(\tilde{y}\right) = \frac{\tilde{S}}{\Lambda + B} \tag{36}$$

For the case of Dirichlet, the final solution is written as:

$$C\left(\tilde{y}\right) = \frac{\tilde{S}}{\Lambda + B}\left[1 - \frac{e^{\sqrt{\Lambda+B}\tilde{y}} + e^{-\sqrt{\Lambda+B}\tilde{y}}}{e^{\sqrt{\Lambda+B}} + e^{-\sqrt{\Lambda+B}}}\right] \tag{37}$$

4.3. Mesh and parameters

The geometry described above for the 2D tube is easily reproducible in OpenFOAM, as a single solid element. The values of the parameters employed in the definition of the mesh are reported in Table 1, and the corresponding output can be seen in Fig. 4.

Initial conditions for the system are those of uniform temperature over the whole domain and fixed pressure gradient along the x direction. Velocity is initialized with a uniform value equal to the expected average value of the parabolic profile. For the single-phase simulations, the phase fraction of the salt is initialized to unity, and the one of the gas is null. Finally, the concentration of xenon in the system is starting from zero. The two-phase simulations are performed starting from the profiles obtained from the corresponding single-phase ones. A uniform non-null value of gaseous fraction (1%) is set inside the domain as initialization for the two-phase simulation. No-slip conditions are set for the velocity at the walls. For the concentrations of xenon in liquid and gaseous phases, Dirichlet conditions are applied at the inlet and outlet boundaries in all cases, while for the upper and the lower walls both Dirichlet and Neumann conditions are employed, depending on the actual simulation performed. The values of the relevant thermophysical properties of the system are chosen to satisfy different constraints of the formulation. The values for the diffusivity of Xe in the salt and of the Henry coefficient are taken from the technical reports of ORNL (Kedl and Houtzeel, 1967). A small value of viscosity is chosen for the gaseous phase, so that the diffusion terms can be neglected in the relative equation. Other useful terms are selected to obtain a significant mass transfer, with the aim of speeding up the process. The main parameters

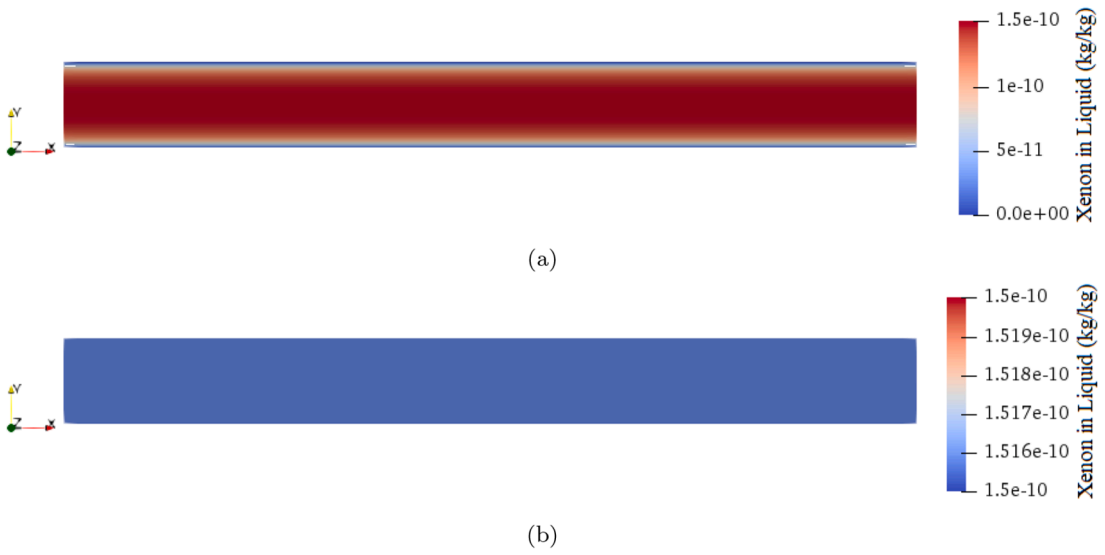

Fig. 5. Xe concentration for single-phase simulations. (a) Dirichlet boundary conditions (b) Neumann boundary conditions.

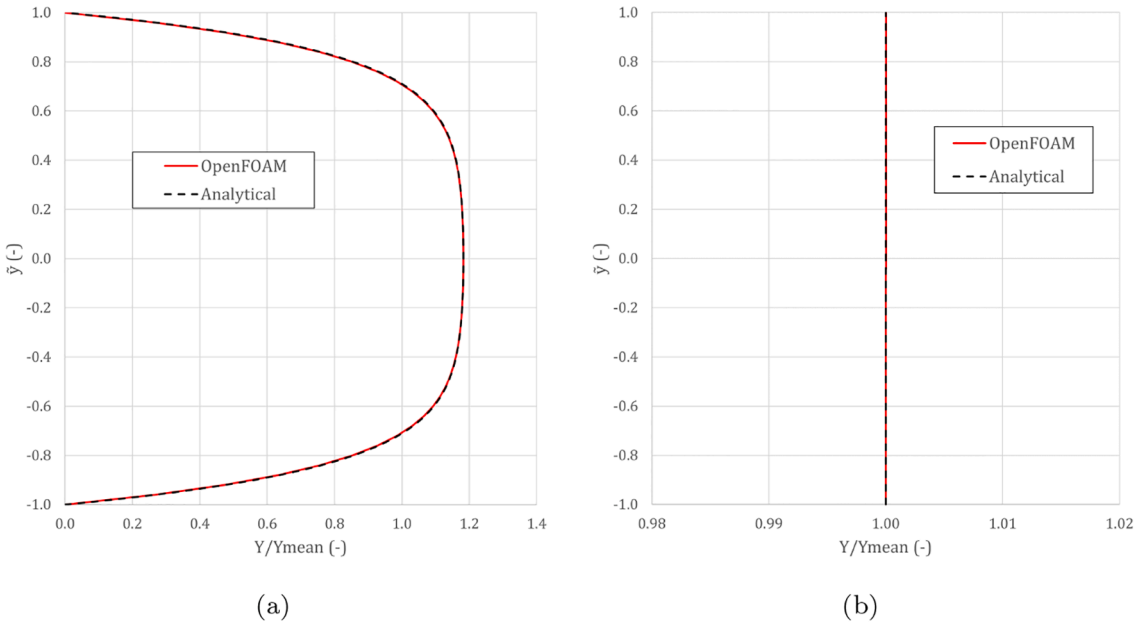

Fig. 6. Xe concentration profiles for transverse section at $x = L/2$, comparison between analytical results and OpenFOAM simulations, single-phase case. (a) Dirichlet boundary conditions (b) Neumann boundary conditions.

are reported in Table 2.

4.4. Results

Results gathered from the simulations of the single-phase cases of Dirichlet and Neumann boundary conditions are reported, respectively, in Fig. 5a and b.

The graphs in Fig. 6a and b display the profile of xenon concentration in the salt for the single-phase case, for a transverse section of the geometry placed at the half-length of the longitudinal axis. A comparison between values predicted from the analytical derivation and the results from the simulations is visible as well. The data presented show very good agreement with the predicted values from the calculations. The mean relative error for the values considered is of 0.53 % with Dirichlet conditions and of 0.002 % with Neumann conditions, possibly deriving from mesh and discretization errors.

Very good agreement is found also for the two-phase case in terms of comparison between numerical output and the analytical calculations, as reported in Fig. 7. The mean relative errors are, for the two-phase cases, of 1.5 % and 0.026 %, for the Dirichlet and Neumann conditions respectively. It is worth pointing out that in the case of the two-phase formulation, with the Dirichlet boundary conditions, the analyses performed put in evidence a different characteristic time for steady-state convergence of the xenon profiles between the two phases. While the concentration in the liquid phase is accurately obtainable with a short simulation time, the evolution needs to go on for a longer time, driven by the dynamics of the gaseous phase, before the true stationary values are reached. Details on the simulation time and computational cost of the simulations are reported in Table 3.

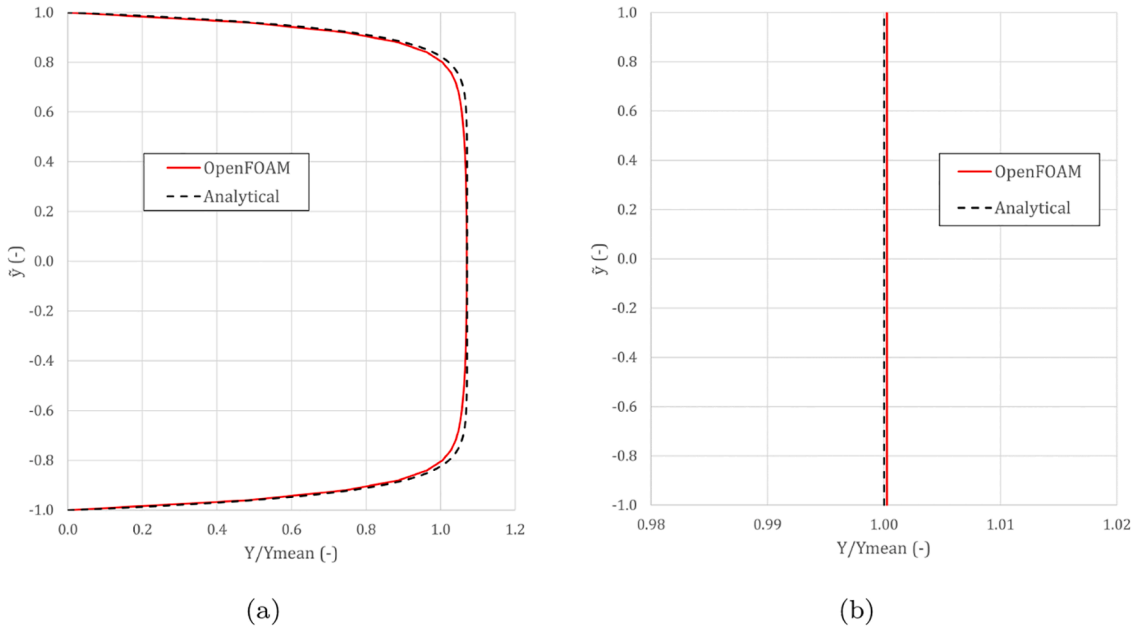

Fig. 7. Xe concentration profiles for transverse section at $x = L/2$, comparison between analytical results and OpenFOAM simulations, two-phase case. (a) Dirichlet boundary conditions (b) Neumann boundary conditions.

Table 3
Computational cost of the analytical simulations.

Case of study	Simulated time	Time cost	System used
Single-phase – Neumann	100000 s	7107 s	Intel Core i7-4710HQ CPU @ 2.5 GHz (4 MPI parallel threads)
Single-phase – Dirichlet	100000 s	6500 s	
Two-phase – Neumann	50000 s	78420 s	Intel Xeon E5-2630 v3 CPU @ 2.4 GHz (4 MPI parallel threads)
Two-phase – Dirichlet	150000 s	227958 s	

Table 4
Main parameters of the MSFR.

Parameter	Value	Units
Nominal power	3000	MW_{th}
Fuel inlet temperature	923	K
Fuel outlet temperature	1023	K
Total salt volume	18	m^3
Fuel composition (% mol)	LiF (77.5) - ThF_4 (20.0) - $^{233}UF_4$ (2.5)	

5. Reactor simulations

In the analysis of a nuclear reactor system, the assessment of the source term is a crucial aspect since it involves both safety and radiation protection issues. In the case of the MSFR, this analysis is more peculiar due to the specific characteristics of this system where the fission products flow with the fuel/coolant mixture. In the MSFR, flows from the core to the off-gas system or to the fuel treatment unit are also foreseen (Delpech et al., 2009). The bubbling system plays a peculiar role in the MSFR, being responsible of the removal of the gaseous and metallic fission product from the core. Being this effect strictly related to the bubble distribution in the core as well as to the mass transfer mechanisms of various sorts, the multiphysics approach represents a suitable tool for the analysis of such a system. In this Section, some simulations are performed following the modelling approach described earlier, aimed at assessing the efficiency of the bubbling system through the calculation of removal rates and characteristic times of GFP concentration in the fuel salt, both 2D and 3D geometries. The main design parameters of the MSFR, considered for these analyses, are reported in Table 4.

5.1. Geometry

As a first approach, a simplified 2D axial-symmetric cylindrical geometry is adopted, rather than a complete 3D model of the reactor, following the work of the past EVOL project (Brovchenko et al., 2013). The presence of solid parts in the system is neglected, and only the liquid salt and the gaseous helium bubbles are taken into account. The geometry is represented in Fig. 8a, with indications about the helium bubbling system, together with the placement of heat exchanger and pump, modelled by means of suitable spatially-confined source/sink terms in the energy and momentum equations. In the upper part of the hot leg, a free surface is simulated to allow for the expansion of the mixture. The computational mesh considered in the simulations is shown in Fig. 8b, and it counts a total of 22671 elements.

The simple geometry allows performing many tests on the behavior of the helium bubbling system and its effect on the gaseous fission products, without the need for excessive computational power. On the other hand, however, the results are not sufficient to correctly depict the complex system that is the MSFR core, and a full 3D analysis must be performed. Additional simulations are thus conducted on a 3D model of a quarter of the full scale MSFR reactor. Just as in the 2D case, only the fluid part of the system is considered. The bubbling system, the heat exchanger and the pumps are simulated as aforementioned. Fig. 9a displays a lateral view of the domain with the same indications of the previous example, and the 3D mesh employed, composed by 1954024 cells, is shown in Fig. 9b.

5.2. Helium bubbling system efficiency

The helium bubbling system is an apparatus envisaged to enhance the removal of the fission products in the core both in gaseous and metallic form. It is thus of critical importance, in the development of the

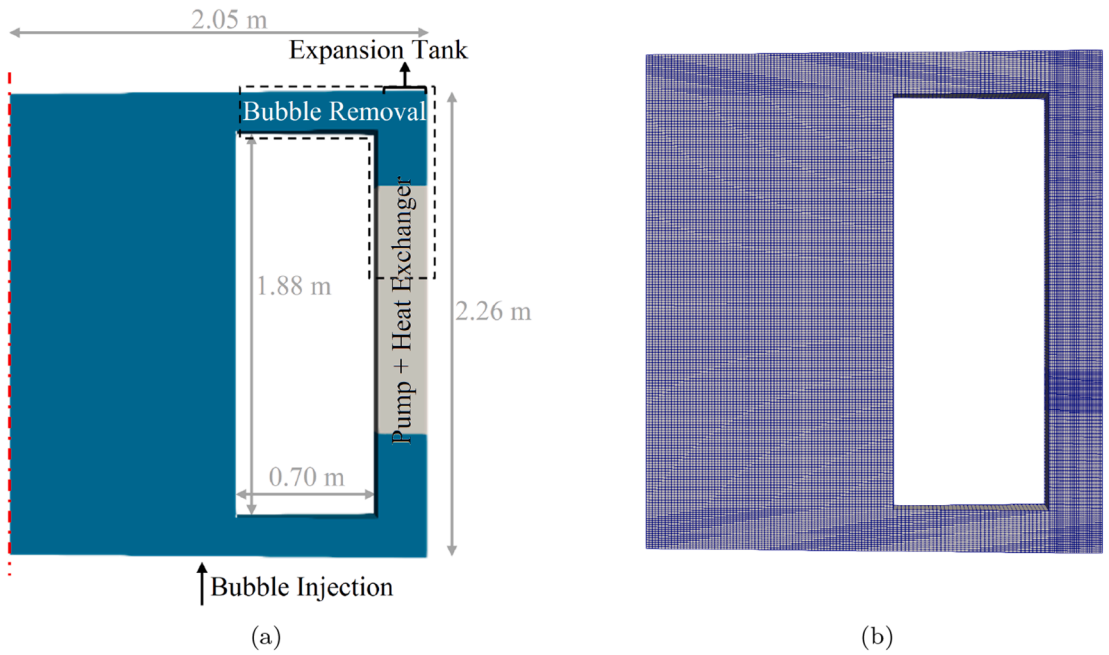

Fig. 8. (a) Geometry and (b) Computational mesh employed for 2D simulations.

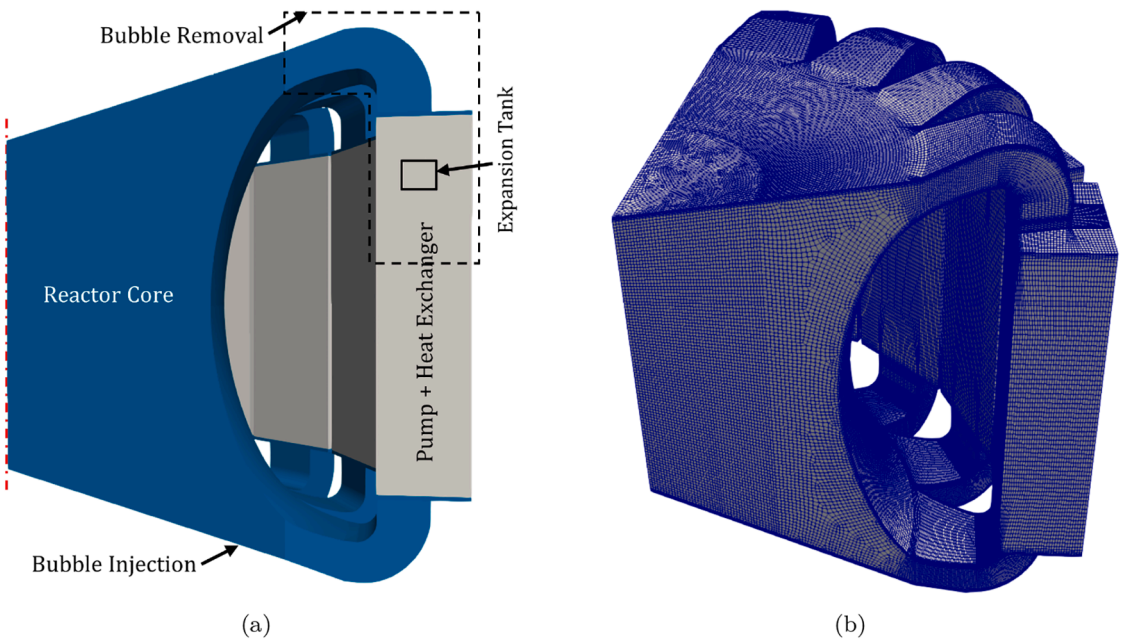

Fig. 9. (a) Geometry and (b) Computational mesh employed for 3D simulations.

reactor, to assess the effectiveness of the helium bubbles in their task. The latter needs also to be accounted for the burnup analysis of the MSFR. The influence on the fuel evolution of the reprocessing treatments is usually tackled in the burnup codes by adding terms in the Bateman equations (Aufiero et al., 2013). As for the helium bubbling, this leads to the introduction of a linear, diagonal (i.e., proportional to the nuclide concentration) term in the differential balance equations as an additional removal contribution. The corresponding simplified analytical expression is:

$$\frac{\partial N}{\partial t} = \left(\nu\Sigma_f - \sigma_a N\right)\phi - \gamma_{bub} N \tag{38}$$

where, for the generic nuclide with concentration N, the term $\nu\Sigma_f\phi$ represents the production from fission, and the terms $\sigma_a N\phi, \lambda_{dec} N$ and $\gamma_{bub} N$ represent the consumption through, respectively, generic absorption reactions, decay and the effect of the bubbling system.

To express the efficiency of the bubbling system in the removal of the fission products, the decay constant γ_{bub} - or its reciprocal τ, representing the characteristic cycle time of the removal process - is defined. For an efficient GFP removal, the removal term defined by γ_{bub} needs to be sufficiently larger than the decay and capture terms. For this reason, a value for the characteristic time around 30 s was selected in earlier studies (Aufiero et al., 2013). One of the objectives of this study is to verify the reliability of this assumption by means of CFD simulation,

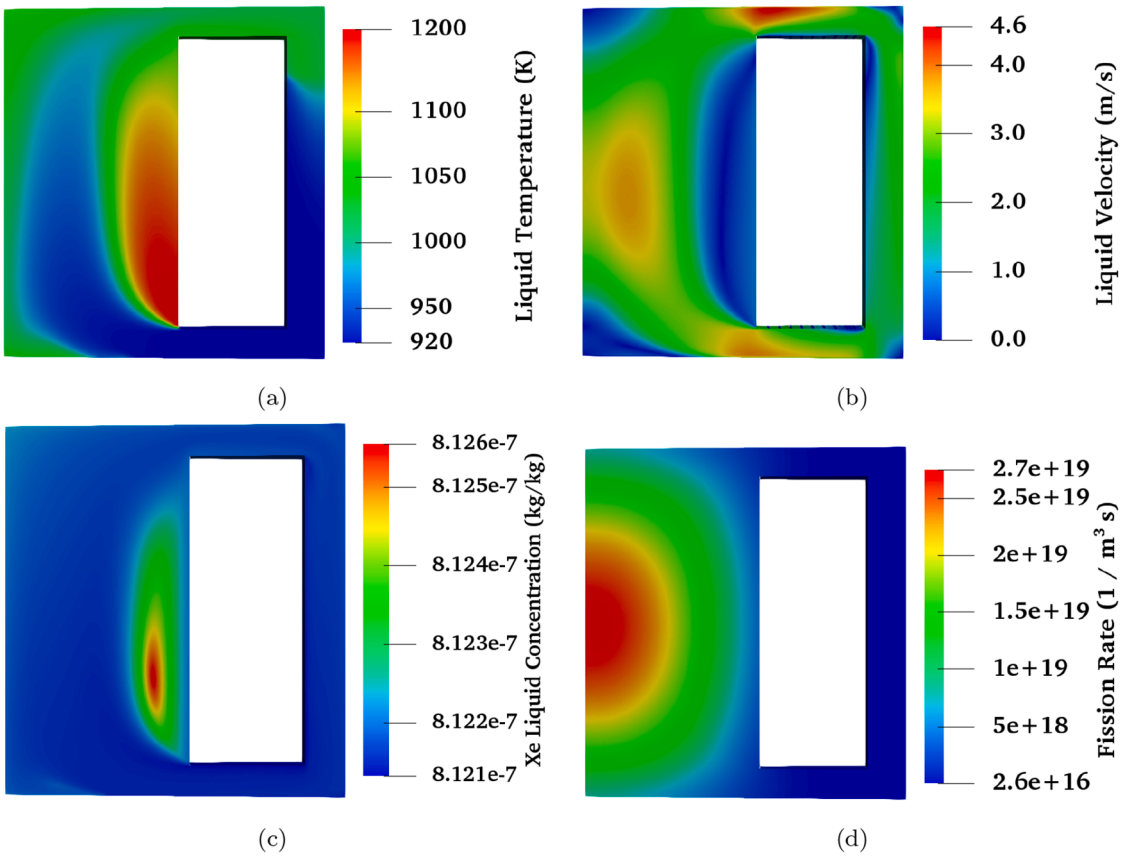

Fig. 10. Color map plots for the profiles of the main quantities in 2D simulations. (a) Temperature (b) Velocity (c) Xe concentration (d) Fission Rate.

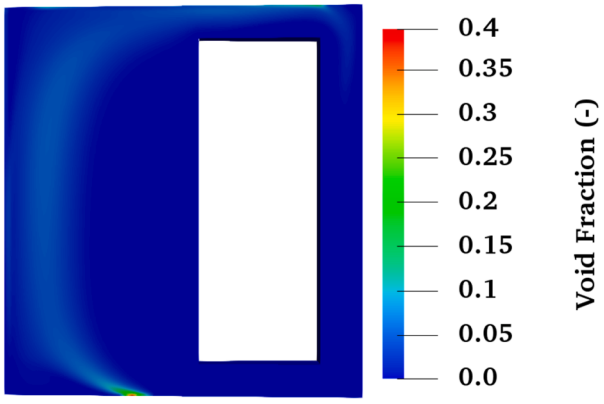

Fig. 11. Void fraction profile for the reference case.

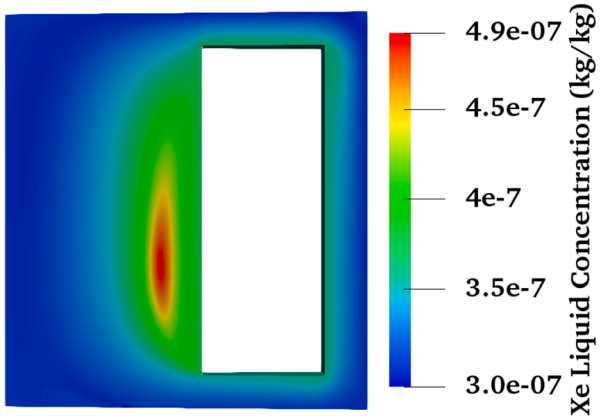

Fig. 12. Xenon concentration profile at the end of the reference simulation.

considering the real bubble distribution and all the relevant transport mechanisms.

The inventory of xenon in the system is calculated as a numerical output of the simulations, by integrating the concentration over the domain. The removal of the gaseous phase from the system is modeled in the solver by the introduction of a continuous implicit sink term in the continuity equation, in a selected region of the domain, proportional to the local gas fraction. In this work, the action of the remover is confined to the hot leg of the reactor, directly past the core outlet. The resulting effect is sufficient to extract all the gas located in the external circuit, so that there are virtually no bubbles re-entering the core from the cold leg. The removal rate can be obtained from the difference between values of xenon inventory at two consecutive time frames, with the additional source term accounting for xenon production:

$$\dot{Xe}_{outflow}\left(t\right) = -\frac{Xe_{mass}(t) - Xe_{mass}(t-\Delta t)}{\Delta t} + S_{Xe} \tag{39}$$

This expression is valid on the assumption that both the decay and the neutron capture on xenon give negligible contributions with respect to the removal through the bubbles. A comparison among the characteristic parameters of the phenomena is presented together with the results, in order to justify this hypothesis.

With these data at hand, the necessary parameter γ_{bub} is directly calculated at every time-step, as the ratio between the extraction rate and the inventory:

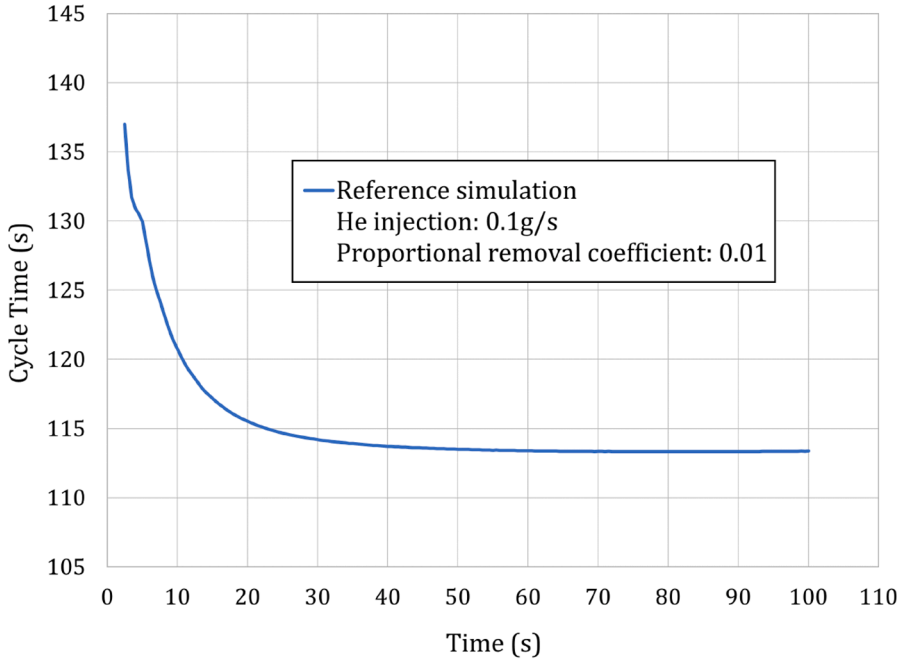

Fig. 13. τ trend in time for the reference case.

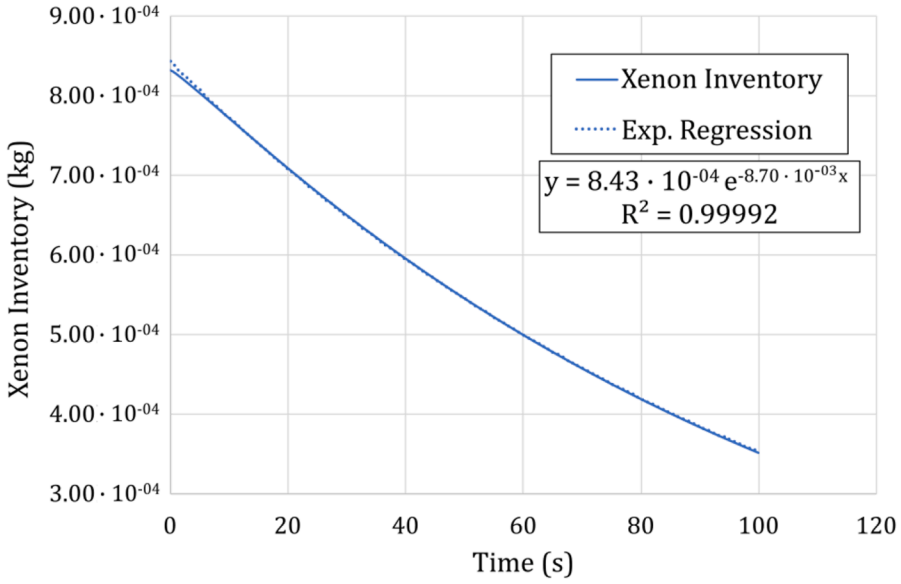

Fig. 14. Xenon inventory trend in time for the reference case, with exponential regression.

Table 5
Comparison among characteristic parameters of xenon consumption phenomena.

Helium bubbling (γ_{bub})	Decay (λ_{dec})	Neutron Capture ($\sigma_c\varphi$)
$8.7 \cdot 10^{-3}\ s^{-1}$ (reference case)	$2.11 \cdot 10^{-5}\ s^{-1}$ (half-life of 9.14 h)	$1.5 \cdot 10^{-9}\ s^{-1}$ (maximum value)

$$\frac{\dot{Xe}_{outflow}\left(kg/s\right)}{Xe_{mass}\ (kg)} = \frac{\gamma_{bub} Xe_{mass}}{Xe_{mass}} = \gamma_{bub}\left(1/s\right) \tag{40}$$

The aforementioned cycle time can be obtained as reciprocal of this quantity:

$$\tau = \frac{1}{\gamma_{bub}} = \frac{Xe_{mass}}{\dot{Xe}_{outflow}} \tag{41}$$

5.3. 2D Model

At first, simulations are performed to find single-phase stationary conditions for the system, starting from conditions of uniform velocity, temperature, pressure and neutron fluxes, and a null concentration of

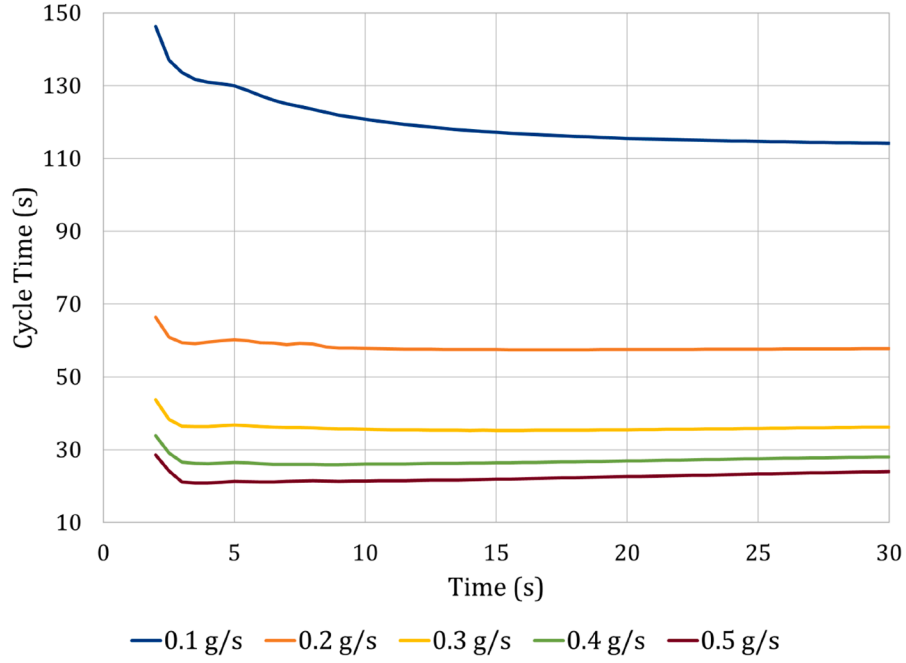

Fig. 15. τ trends in time for different values of helium inlet flow rate.

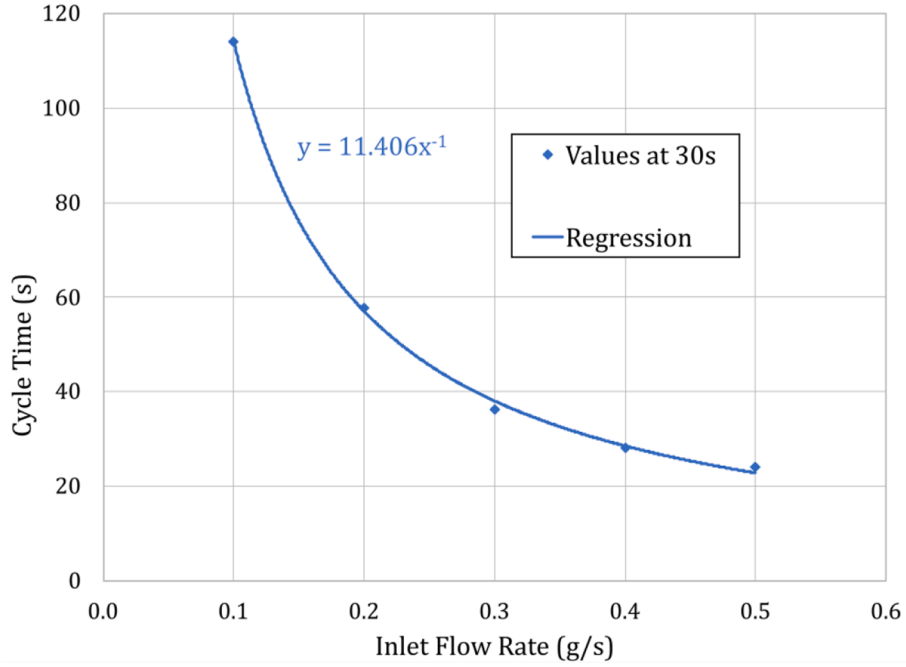

Fig. 16. τ trend as a function of helium inlet flow rate, with evidence of inverse proportionality.

Table 6
Values of τ for increasing helium inlet flow rate, with evidence of inverse proportional behavior.

Flow rate (g/s)	τ at 30 s (s)	$\tau_i/\tau_{0.1}$ (-)
0.1	114.1898	1.000
0.2	57.7598	0.506
0.3	36.1896	0.317
0.4	28.0355	0.245
0.5	23.9782	0.210

xenon in the system. No-slip boundary conditions are chosen for the velocity fields at the reactor walls and atmospheric pressure is imposed at the free surface in the upper right corner. Neumann conditions are applied for temperature and precursors (for both neutrons and decay heat), and for the neutron fluxes albedo boundary conditions are employed, as mentioned in the previous Sections. Fig. 10 shows the color map plots of the obtained quantities of main interest. As it is evident from the temperature and velocity fields (Fig. 10a and b), a stagnation zone is formed close to the blanket wall, where xenon tends also to be accumulated (Fig. 10c). This phenomenon is of great

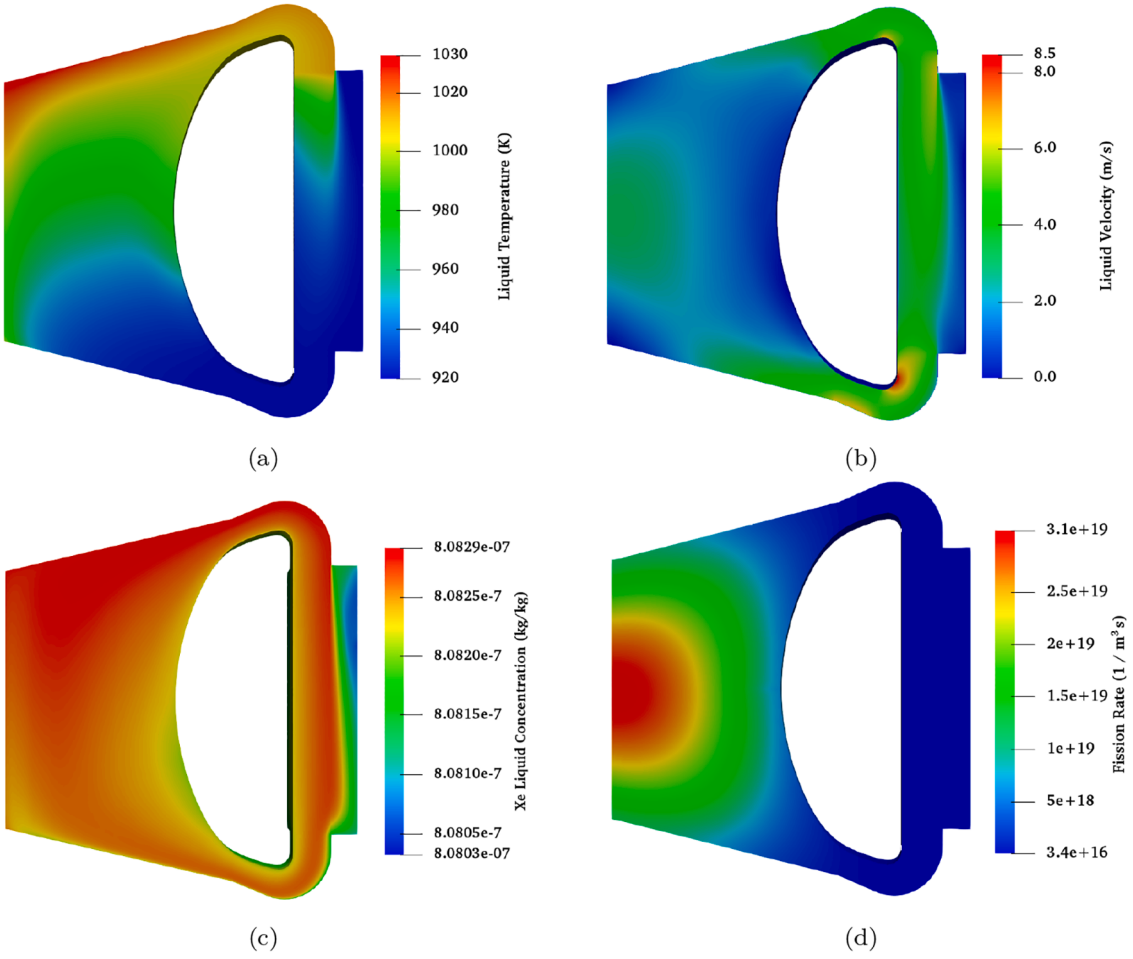

Fig. 17. Color map plots for the single-phase steady-state conditions found for the 3D model of a quarter of the reactor (vertical sections). (a) Temperature (b) Velocity (c) Xenon concentration (d) Fission rate.

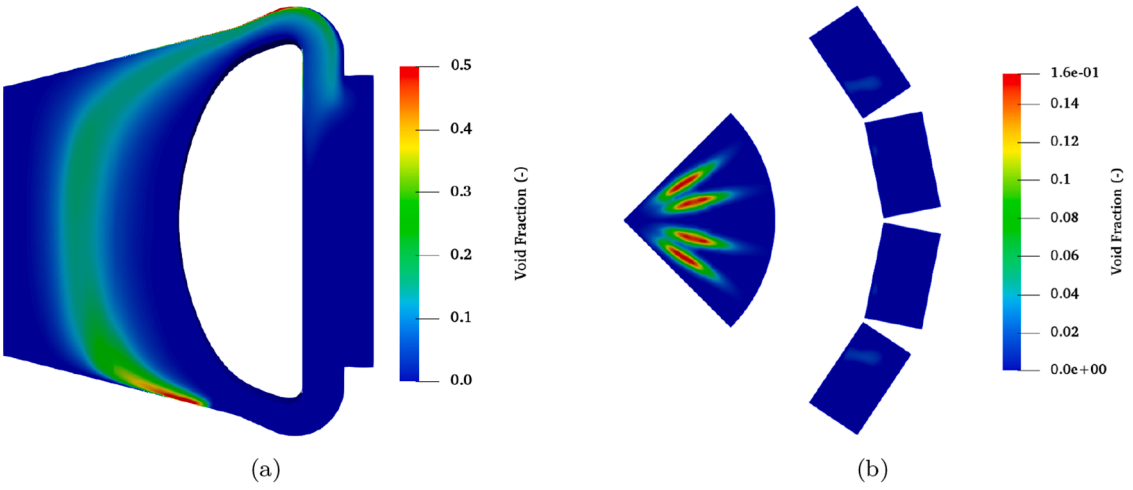

Fig. 18. Void fraction profile for the quarter of the reactor. (a) Vertical section (b) Horizontal section.

importance because it can worsen the ability of the bubbles to remove the gaseous fission products from the mixture, especially for species with a low value of diffusivity in the salt.

The single-phase steady-state results are then taken as starting point for the two-phase simulations, employing the same boundary conditions. During the simulations, after a short initial transient of a few seconds, the gaseous phase fraction reaches the steady-state distribution displayed in Fig. 11. From the plot, the path of the bubbles can be clearly observed: they are injected from the bottom of the core and get transported by the salt up top to the hot leg, where they are removed. During their flow, the bubbles are able to extract xenon from the salt through mass transfer. The resulting effect on the concentration of Xe-135 can be

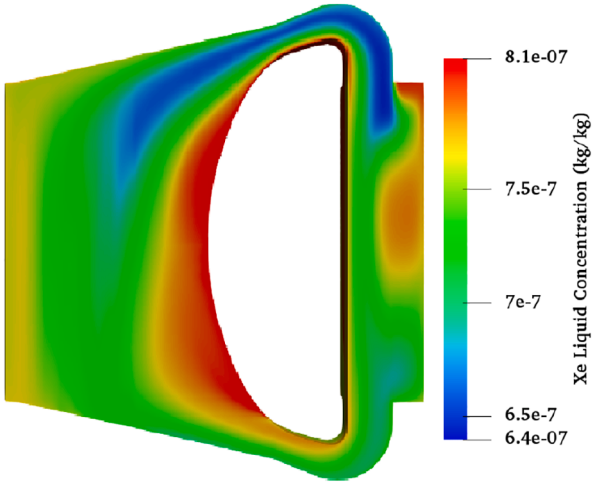

Fig. 19. Xenon concentration profile for the quarter of the reactor after injection of helium.

seen by the comparison between the single-phase steady-state plot of Figs. 10c and 12 down below, which corresponds to the distribution of xenon mass fraction in the salt at the end of the two-phase reference simulation, i.e., after 100 s. The overall reduction is of a factor of about 2.3. It should however be pointed out that this is not the final stationary profile for the concentration in presence of the bubbling flow, and the simulation time needed to reach the steady-state conditions is much longer. On the other hand, 100 s are more than sufficient to calculate the cycle time defined by Eq. (41) and taken as main figure of merit of the efficiency of the helium bubbling system.

Fig. 13 displays a plot of its trend in time, together with indications about the conditions chosen to model the helium bubbling in the reference simulation.

As shown, the curve reaches, after an initial steep transient, a flat profile. Reaching a constant value of cycle time translates also in a constant value for the bubbling constant γ_{bub} of Eq. (40), which is in fact the reciprocal of the cycle time. This fact confirms the prior hypothesis made in employing an exponential behavior analogous to the radioactive decay to model the effect of the helium bubbling system on the removal of fission products. Another confirmation comes from Fig. 14, where an exponential fit is performed on the time evolution of the xenon inventory in the system. The coefficient in the exponential term found through the data fitting turns out to be almost identical to the bubbling constant γ_{bub}. This analysis verifies both the suitability of modelling the bubbling system through a linear, diagonal term in the Bateman equations and the formulation adopted to calculate the cycle time, i.e., neglecting the decay and the transmutation terms with respect to the removal effect of the helium bubbling.

As further proof that the other phenomena of consumption of xenon are negligible with respect to the removal through the helium bubbling system, Table 5 displays a comparison among indicative values of the respective characteristic parameters.

The variation of the cycle time for different values for inlet flow rate of gaseous phase was also investigated. Keeping as the reference case the results obtained with a flow rate of 0.1 g/s, other simulations were performed varying the parameter (using values of 0.2–0.3–0.4 and 0.5 g/s). The comparison among the obtained trends of cycle time is shown in Fig. 15.

Table 7
Computational cost of the reactor simulations.

Case of study	Simulated time	Time cost	System used
2D - Single Phase	40000 s	18412 s	Intel Core i7-4710HQ CPU @ 2.5 GHz (4 MPI parallel threads)
2D - 0.1 g/s inlet	100 s (Δt 1 ms)	48386 s	
2D - 0.2 g/s inlet	30 s (Δt 1 ms)	14276 s	
2D - 0.3 g/s inlet	30 s (Δt 1 ms)	14589 s	
2D - 0.4 g/s inlet	30 s (Δt 1 ms)	14849 s	
2D - 0.5 g/s inlet	30 s (Δt 1 ms)	15225 s	
3D - Single Phase	20000 s	108678 s	Intel CascadeLake 8260 CPU @ 2.4 GHz (36 MPI parallel threads)
3D - Two Phase	6 s (Δt 0.1 ms)	294965 s	

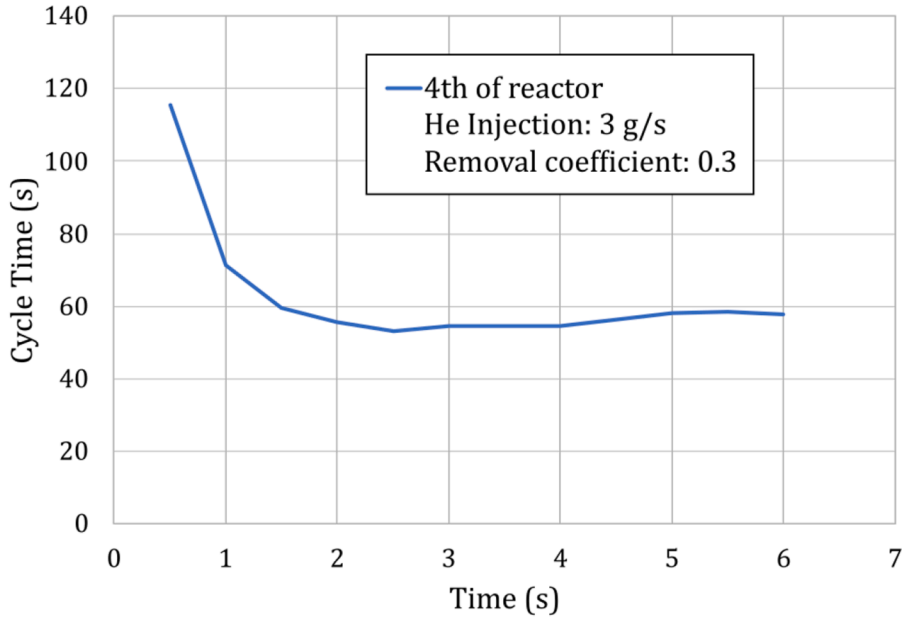

Fig. 20. τ trend in time for the 3D case (quarter of the reactor).

Some elements can be observed and analyzed from this graph. First, the initial steep transient is for all cases shorter with respect to the one obtained for the reference case. Then, the effect of the stagnation zone for xenon can be noticed looking at the two curves with the highest values of flow rate, 0.4 and 0.5 g/s. The increasing trend of τ for these two can be interpreted as a consequence of the fact that the helium bubbles are not able to reach the whole core volume, and thus the mass of xenon in the stagnation zone is not affected by them. This leads to the observable increase of cycle time, whereas in the case where the helium flow can interact with xenon in the entire geometry, the value of cycle time would remain constant as the simulation progresses. The effect is not seen for the lower values of flow rate employed because it would need longer simulation times to manifest evidently.

Fig. 15 also shows that the dependence of the cycle time from the inlet flow rate corresponds to a behavior of inverse proportionality. In order to highlight this result, Fig. 16 displays, for the different magnitudes of helium injection, the values of cycle time obtained from the simulations after 30 s of time. The curve is fitted against an inverse linear model, showing good agreement overall. The proportionality trend is further evident from the numerical data reported in Table 6.

The results just displayed show that the order of magnitude of tens of seconds presented by the SAMOSAFER designers as hypothesis of the characteristic time of removal of the gaseous fission products is verified by CFD simulations. The reference value of 30 s is also obtainable, depending on the value for the inlet helium flow rate employed. In particular, the results of the analyses show that, for the simplified 2D model, a cycle time of 30 s is achieved with a flow rate between 0.3 and 0.4 g/s.

5.4. 3D model

After the collection of extensive results from the simulations of the simplified 2D model, a test on a complete 3D model was performed, in order to verify the up-scaling capabilities of the new features implemented in the code and to get some preliminary results on the helium bubbling efficiency in the present configuration, represented as a quarter of the full-scale MSFR system (Cervi, 2020). The simulations are performed analogously to the 2D example, finding initially the stationary single-phase conditions and starting the two-phase simulations from those. For what concerns boundary conditions and empirical correlations employed in the modelling of the various phenomena, the same choices made for the 2D model were followed, both for the thermal–hydraulics and the neutronics of the system. The main profiles of interest for the single-phase steady-state conditions are displayed in Fig. 17.

As it can be seen, the profiles present some differences with respect to the ones obtained for the 2D case. In particular, the refined curved design of the 3D geometry prevents the formation of the previously mentioned stagnation zone, modifying the temperature and velocity profiles in particular. As already stated, this factor can be also of importance in the removal of xenon, since in this case the helium bubbles are facilitated in reaching the entire volume of the core.

For the two-phase simulations, bubble injection and extraction are modelled as displayed in Fig. 9a. The obtained distribution for the void fraction in the core is displayed in Fig. 18, both for a vertical section of a single leg, and for a horizontal one, displaying the condition of the whole reactor core. Fig. 19 shows the corresponding profile of xenon concentration with the effect of helium injection.

The graph in Fig. 20 displays the trend in time for the cycle time of Eq. (41), together with information about the inlet flow of helium and the extraction rate of the gaseous phase employed for the simulation. The value obtained for the cycle time is in the same order of magnitude of the results of the 2D simulations, acting as confirmation of the validity of the previous analyses and verification of the up-scaling capabilities of the implemented model.

As it can be seen from the graph, the simulated time for the 3D model was not very long, even if the initial transient is much shorter than the 2D case and the τ is seen to reach already a value which remains almost constant in time.

The computational cost of all the simulations performed for the 2D and 3D geometries are reported in Table 7.

6. Conclusions

The work presented in this paper extends the capabilities of state-of-the-art MSFR multiphysics tools to the analysis of the behavior of the Gaseous Fission Products. The newly implemented features enable the simulation of the production, transport and consumption of GFPs inside the fuel salt, as well as the migration of such species from the liquid mixture to the gaseous phase. Gas is injected in the reactor by the helium bubbling system, and is extracted by forced removal to mimic the effect of the off-gas system. All transport mechanisms are modelled based on the local liquid/gas phase distributions following a Euler-Euler multiphase CFD approach.

The developed models have been first verified against analytical results on a simplified geometry, and then tested on 2D and 3D MSFR case studies, displaying the new capabilities of the solver to study the impact of the bubbling system on the mass balance of the gaseous fission products. Xe-135 has been employed as reference nuclide for the analysis, but the results are easily extendable to any specie of interest. The results of the simulations performed on the 2D simplified geometry demonstrate the efficiency of the removal of GFPs through helium bubbling, suggesting a direct proportionality of such efficiency to the inlet helium flow rate. Additionally, numerical results show a characteristic cycle time estimated by means of CFD simulations in the order of tens of seconds for all the considered cases, in substantial agreement with values assumed in earlier studies. The influence of the gaseous phase on neutronics in terms of associated reactivity effects, however, could prevent the use of sufficiently large inlet flow rates, but more detailed analyses will be needed for an accurate assessment. Finally, the simulation carried out on the 3D model helped verifying the up-scaling capabilities of the solver and confirming the results obtained from the analyses of the simplified 2D geometry.

This work constitutes a step forward in the study of the MSFR concept. Further developments on the study of the helium bubbling system include, for instance, the simultaneous study of multiple gaseous fission product species, with the aim of correctly estimating the flows going from the core to the off-gas system and the source term. Additionally, different models and correlations for the mass transfer terms should be properly tested. Finally, the effect of GFPs and of helium bubbling on the transport of solid fission products has to be investigated as well.

Research data

The data that support the findings of this study are openly available in Zenodo at http://doi.org/10.5281/zenodo.5156540.

Funding

This project has received funding from the Euratom research and training programme 2014–2018 under grant agreement No. 847527.

Disclaimer

The content of this paper does not reflect the official opinion of the European Union. Responsibility for the information and/or views expressed therein lies entirely with the authors.

Declaration of Competing Interest

The authors declare that they have no known competing financial

interests or personal relationships that could have appeared to influence the work reported in this paper.

References

Aufiero, M., Cammi, A., Fiorina, C., Leppänen, J., Luzzi, L., Ricotti, M.E., 2013. An extended version of the SERPENT-2 code to investigate fuel burn-up and core material evolution of the Molten Salt Fast Reactor. J. Nucl. Mater. 441, 473–486.

Betzler, B., Heidet, F., Feng, B., Rabiti, C., Sofu, T., Brown, N., 2019. Modeling and simulation functional needs for molten salt reactor licensing. Nucl. Eng. Des. 355.

Brovchenko, M., Merle Lucotte, E., Rouch, H., Alcaro, F., Allibert, M., Aufiero, M., Cammi, A., Dulla, S., Feynberg, O., Frima, L., Geoffroy, O., Ghetta, V., Heuer, D., Ignatiev, V., Kloosterman, J.L., Lathouwers, D., Laureau, A., Luzzi, L., Merk, B., Ravetto, P., Rineiski, A., Rubiolo, P., Rui, L., Szieberth, M., Wang, S., Yamaji, B., 2013. Optimization of the pre-conceptual design of the MSFR. Deliverable 2, 1–69.

Cammi, A., Di Marcello, V., Guerrieri, C., Luzzi, L., 2011. Transfer Function Modeling of Zero-Power Dynamics of Circulating Fuel Reactors. J. Eng. Gas Turbines Power 133.

Cervi, E., 2020. An Innovative Multiphysics Modelling Approach for the Analysis and the Development of the Generation IV Molten Salt Fast Reactor. Ph.D. thesis. Politecnico di Milano.

Cervi, E., Lorenzi, S., Cammi, A., Luzzi, L., 2017. An Euler-Euler multi-physics solver for the analysis of the helium bubbling system in the MSFR. In: NENE 2017 26th International Conference Nuclear Energy for New Europe, Bled, Slovenia, September 11–14, 2017.

Cervi, E., Lorenzi, S., Cammi, A., Luzzi, L., 2019. Development of a multiphysics model for the study of fuel compressibility effects in the Molten Salt Fast Reactor. Chem. Eng. Sci. 193, 379–393.

Cervi, E., Lorenzi, S., Cammi, A., Luzzi, L., 2019. Development of an SP3 neutron transport solver for the analysis of the Molten Salt Fast Reactor. Nucl. Eng. Des. 346, 209–219.

Cervi, E., Lorenzi, S., Luzzi, L., Cammi, A., 2019. Multiphysics analysis of the MSFR helium bubbling system: a comparison between neutron diffusion, SP3 neutron transport and Monte Carlo approaches. Ann. Nucl. Energy 132, 227–235.

Delpech, S., Merle-Lucotte, E., Heuer, D., Allibert, M., Ghetta, V., Le-Brun, C., Doligez, X., Picard, G., 2009. Reactor physic and reprocessing scheme for innovative molten salt reactor system. J. Fluorine Chem. 130, 11–17.

Di Ronco, A., Lorenzi, S., Giacobbo, F., Cammi, A., 2021. An eulerian single-phase transport model for solid fission products in the molten salt fast reactor: Development of an analytical solution for verification purposes. Front. Energy Res. 9.

Engel, J., Steffy, R., 1971. Xenon Behavior in the Molten Salt Reactor Experiment. Technical Report. Oak Ridge National Laboratory (ORNL). Oak Ridge, TN (United States).

Fiorina, C., Lathouwers, D., Aufiero, M., Cammi, A., Guerrieri, C., Kloosterman, J.L., Luzzi, L., Ricotti, M.E., 2014. Modelling and analysis of the MSFR transient behaviour. Ann. Nucl. Energy 64, 485–498.

Higbie, R., 1935. The rate of absorption of a pure gas into still liquid during short periods of exposure. Inst. Chem. Eng. 35, 36–60.

Ishii, M., Hibiki, T., Ishii, M., Hibiki, T., 2011. Two-fluid model. In: Thermo-Fluid Dynamics of Two-Phase Flow. Springer, New York, pp. 155–216.

Kedl, R., Houtzeel, A., 1967. Development of a Model for Computing 135Xe Migration in the MSRE. Technical Report. Oak Ridge National Laboratory (ORNL). Oak Ridge, TN (United States).

Lathouwers, D., 1999. Modelling and Simulation of Turbulent Bubbly Flow. Ph.D. thesis. Technische Universiteit Delft.

Leppänen, J., Pusa, M., Viitanen, T., Valtavirta, V., Kaltiaisenaho, T., 2015. The Serpent Monte Carlo code: status, development and applications in 2013. Ann. Nucl. Energy 82, 142–150.

Marschall, H., 2011. Towards the Numerical Simulation of Multi-Scale Two-Phase Flows. undefined, 322.

Peebles, F.N., 1968. Removal of Xe-135 from Circulating Fuel Salt of the MSBR by Mass Transfer to Helium Bubbles. Technical Report. Oak Ridge National Laboratory (ORNL). Oak Ridge, TN (United States).

Polyanin, A., Zaitsev, V., 2002. Handbook of Exact Solutions for Ordinary Differential Equations, Second Edition.

Price, T., Chvala, O., Bereznai, G., 2020. A dynamic model of xenon behavior in the molten salt reactor experiment. Ann. Nucl. Energy 144, 107535.

Price, T.J., Chvala, O., Taylor, Z., 2020. Xenon in molten salt reactors: the effects of solubility, circulating particulate, ionization, and the sensitivity of the circulating void fraction. Nucl. Eng. Technol. 52, 1131–1136.

Ranz, W.E., Marshall, W.R., 1952. Evaporation from drops. Parts I & II. Chem. Eng. Progr. 48, 141–173.

Rhodes, M., 2008. Introduction to Particle Technology, second ed. John Wiley & Sons Ltd., Chichester, UK.

Roelofs, F., Stempniewicz, M., 2021. Molten salt modelling capabilities in spectra and application to msre and mk1-pb-fhr. Nucl. Eng. Des. 381.

Rusche, H., 2002. Computational Fluid Dynamics of Dispersed Two-Phase Flows at High Phase Fractions. Ph.D. thesis. Imperial College of Science, Technology and Medicine.

Santamarina, A., Bernard, D., Rugama, Y., OECD Nuclear Energy Agency., 2009. The JEFF-3.1.1 nuclear data library: JEFF report 22, validation results from JEF-2.2 to JEFF-3.1.1. OECD 2009 NEA No. 6807, ISBN 978-92-64-99074-6, 61.

Schiller, L., Naumann, A., 1933. Über die grundlegenden Berechnungen bei der Schwerkraftaufbereitung. Verein Deutscher Ingenieure 44, 318–320.

Weller, H.G., Tabor, G., Jasak, H., Fureby, C., 1998. A tensorial approach to computational continuum mechanics using object-oriented techniques. Comput. Phys. 12, 620.